

Determination of Venus' interior structure with EnVision

Pascal Rosenblatt¹, Caroline Dumoulin², Jean-Charles Marty³, and Antonio Genova⁴

¹Laboratory of Planetology and Geodynamics

²Université de Nantes

³Groupe de Recherche de Geodesie Spatiale (GRGS)

⁴Massachusetts Institute of Technology

November 22, 2022

Abstract

The Venesian geological features are poorly gravity-resolved and the state of the core is not well constrained, preventing to understand Venus' cooling history. The EnVision candidate mission to the ESA's Cosmic Vision Programme consists of a low-altitude orbiter to investigate geological and atmospheric processes. The gravity experiment aboard this mission aims to determine Venus' geophysical parameters to fully characterize its internal structure. By analyzing the radio-tracking data that will be acquired through daily operations over six Venesian days (four Earth's years), we will derive a highly-accurate gravity field (spatial resolution better than ~ 170 km), allowing to detect lateral variations of the lithosphere and crust properties beneath most of the geological features. The expected 0.3% error on the Love number k_2 , 0.1° error on the tidal phase lag and 1.4% error on the moment of inertia are fundamental to constrain the core size and state as well as the mantle viscosity.

Hosted file

rosenblatt_etal_2020_envision_gravi_supporting_material.docx available at <https://authorea.com/users/535328/articles/598727-determination-of-venus-interior-structure-with-envision>

1
2
3
4
5
6
7
8
9
10
11
12
13
14
15
16
17

Determination of Venus' interior structure with EnVision

Pascal Rosenblatt¹, Caroline Dumoulin¹, Jean-Charles Marty², and Antonio Genova³

¹Laboratoire de Planétologie et Géodynamique, Nantes, France.

²CNES/GRGS, Toulouse, France.

³Sapienza University of Rome, Rome, Italy.

Corresponding author: Pascal Rosenblatt (pascal.rosenblatt@univ-nantes.fr)

Key Points:

- Daily radio tracking data from EnVision over six Venusian days will contribute significantly to determine Venus' gravity field.
- Spatial resolution of the gravity field of at least 170 km but as low as 120 km is achievable with the current mission design.
- Accurate estimate of the gravitational tides and precession rate will allow constraining the core size and state, and mantle viscosity.

18 Abstract

19 The Venusian geological features are poorly gravity-resolved and the state of the core is
20 not well constrained, preventing to understand Venus' cooling history. The EnVision candidate
21 mission to the ESA's Cosmic Vision Programme consists of a low-altitude orbiter to investigate
22 geological and atmospheric processes. The gravity experiment aboard this mission aims to
23 determine Venus' geophysical parameters to fully characterize its internal structure. By
24 analyzing the radio-tracking data that will be acquired through daily operations over six
25 Venusian days (four Earth's years), we will derive a highly-accurate gravity field (spatial
26 resolution better than ~ 170 km), allowing to detect lateral variations of the lithosphere and crust
27 properties beneath most of the geological features. The expected 0.3% error on the Love number
28 k_2 , 0.1° error on the tidal phase lag and 1.4% error on the moment of inertia are fundamental to
29 constrain the core size and state as well as the mantle viscosity.

30

31 Plain Language Summary

32 *Although, Earth and Venus are rocky planets with a similar size, they have evolved very*
33 *differently. A comprehensive knowledge of Venus' geological history helps understanding what*
34 *caused this different evolution. The EnVision orbiter mission candidate to the Medium class*
35 *mission call of the ESA cosmic vision program aims to better characterize the atmospheric*
36 *dynamics, the surface and the interior of the planet from the core to the crust. In this study we*
37 *perform simulations of the EnVision gravity experiment, which is part of the radio science*
38 *experiment, showing that this experiment is a fundamental asset to constrain the state and size of*
39 *the core as well as the mantle viscosity. The expected results of this experiment will provide a*
40 *valuable contribution to our understanding of Venus' geological history.*

41 1 Introduction

42 Why Venus and Earth evolved so differently remains an open issue. The geological
43 history of Venus is the most unknown among the terrestrial planets, preventing to fully
44 understand the processes that led to its current state. The primary objectives of the EnVision
45 mission, candidate to the M5 call of the ESA's Cosmic Vision Programme, are to determine
46 whether Venus is geologically active today, the relationship with its atmosphere, and its interior
47 structure (e.g. Ghail et al., 2019). The knowledge of the planetary interior is needed to better
48 constrain its cooling history (e.g. Mocquet et al., 2011; Smrekar et al., 2018), and so to better
49 constrain its geological evolution. Because of the lack of seismic data, of moon(s) and of a global
50 magnetic field, the unique way to constrain Venus' interior from core to crust is to determine an
51 accurate and well resolved gravity field.

52 The current solution of Venus gravity field was determined from the radio tracking data
53 of the NASA Magellan spacecraft (e.g. Kaula, 1996; Barriot et al., 1998) and additionally of the
54 Pioneer Venus Orbiter (PVO) (e.g. Konopliv and Sjogren, 1996; Konopliv et al., 1999). This
55 recovered gravity field shows a non-uniform spatial resolution ranging from 540 to 170 km,
56 preventing to fully detect the gravity signal induced by lithospheric loads as well as crustal
57 density and thickness variations. To improve the determination of Venus' gravity is then
58 fundamental to better understand the geological history of the planet (e.g. Anderson and
59 Smrekar, 2006). In addition, our knowledge of the tidal component of the gravity field (i.e. the
60 tidal Love number k_2) is limited by an uncertainty of 22% (Konopliv and Yoder, 1996), which is

61 not accurate enough to conclude about the Venus' deep interior structure, e.g. whether the core is
62 solid (viscous) or liquid, what is its size and what is the viscosity of the mantle (Dumoulin et al.,
63 2017). An accurate estimation of these geophysical quantities would help to constrain the cooling
64 history of the planet. Besides, the gravity and the topography data can be used to estimate the
65 crustal and elastic lithosphere thicknesses (e.g. James et al., 2013; Jimenez-Diaz, 2015, Anderson
66 and Smrekar, 2006). However, the spatial resolution of the gravity field solution from Magellan
67 tracking data is below degree and order 70 (270 km) for almost half of the planet, yielding to
68 uncertainties in the crustal and lithosphere structure estimates (Smrekar et al., 2018).

69 The geophysical goals of the radio science experiment aboard EnVision are thus the
70 determination of a uniform high-resolution gravity field to resolve anomalies associated with the
71 geological features across the entire planet. An improved coverage of the planet will allow us to
72 achieve an accuracy of the tidal Love number k_2 better than 3%, which is required to better
73 constrain the Venus' mantle viscosity and composition (iron content) as well as the state of its
74 core, by ruling out some combinations of these parameters in the current models of Venus
75 interior (Dumoulin et al., 2017).

76 Here, we present numerical simulations of the EnVision gravity experiment to assess the
77 quality of the Venus gravity solution that can be reached. Section 2 of this paper presents this
78 experiment as currently designed, Section 3 displays the methodology to simulate this
79 experiment, and Section 4 shows the expected improvement of the Venusian gravity field and of
80 the knowledge of the interior structure of the planet. Section 5 summarizes the main results.

81 **2 The EnVision gravity experiment**

82 The main techniques to determine the gravity field of planets is based on the precise
83 reconstruction of the motion of one or several orbiting spacecraft (e.g. Balmino et al., 1982;
84 Konopliv and Sjogren, 1996; Zuber et al., 2007). The Precise Orbit Determination (POD)
85 process consists in fitting the dynamical model of the spacecraft motion to the radio tracking
86 data. The radiometric data are collected by Earth's based deep space stations (e.g. Holmes et al.,
87 2008) that enable the telecommunications to measure the Doppler shift of the radio-link carrier
88 frequency. The spatial resolution and accuracy of the gravity field solution depends on the
89 precision and coverage of the tracking measurements as well as on the accuracy of the dynamical
90 model, and on the spacecraft orbital altitude.

91 The EnVision spacecraft orbit is an elliptical orbit with an altitude range between 220 km
92 and 515 km and an inclination of 88 degrees allowing for high-resolution mapping of the Venus
93 gravity field. The EnVision gravity experiment relies on the two-way radio-link established on
94 daily passages of at least 3.5 hours long, to guarantee the data download required by the
95 EnVision payload. A very stable reference X-band frequency (at 7.1 GHz) is generated at the
96 ground station and sent to the spacecraft, which then sends back to the station a coherent
97 downlink frequency (X-band at 8.4 GHz) thanks to the radio-transponder of the spacecraft
98 telecommunication system. An additional Ka-band downlink coherent frequency (32 GHz) is
99 also sent back to Earth for supporting the telemetry volume requirements. This two-way X/X-Ka
100 radio-link provide a precise Doppler tracking of the EnVision spacecraft over the six Venusian
101 cycles of the mission science phase.

102 **3 Methodology of simulations**

103 We performed numerical simulations of the EnVision gravity experiment by accounting
104 for a realistic scenario of the gravity experiment.

105 **3.1 EnVision Doppler noise budget**

106 The main source of noise in the X-band Doppler measurements between a Venusian
107 spacecraft and the Earth is the electron content fluctuations of the interplanetary plasma along
108 the propagation path of the radio wave (phase scintillation, Ho et al., 2008). The noise amplitude
109 depends on the Sun-Probe-Earth (SPE) angle: the smaller this angle is, the closer the radio-path
110 to the solar corona is and the larger is the noise. Models enable a characterization of this noise
111 (Deep Space Network, note 202, 2019), but only a multi-frequency link would enable a full
112 calibration (e.g. Iess et al., 2014). The EnVision tracking system provides a dual frequency on
113 the downlink only, thus the plasma noise on the uplink remains. A floor value of 0.027 mm/s at
114 10 seconds Doppler count time is reached around inferior conjunctions (i.e. Venus is between the
115 Sun and the Earth, Table S1), then increases toward superior conjunctions (i.e. the Sun is
116 between the Earth and Venus), as a dominant source in the Doppler noise budget at SPE angles
117 lower than 20 degrees (i.e. > 0.1 mm/s, see Table S1). Solar conjunctions occur with a synodic
118 period of 584 Earth's days, therefore two or three periods during the mission timespan (i.e. 1458
119 Earth's days) will be characterized by high radio tracking noise, depending on the mission
120 starting date with respect to the first superior conjunction (Figure S1).

121 In addition to the interplanetary plasma, other sources of propagation noise have to be
122 taken into account, due to the charged particles of the Earth's ionosphere and to the propagation
123 delay in the neutral atmosphere (troposphere). A calibration system using GNSS technics at the
124 ESTRACK ground stations allows to correct the tropospheric effect with a residual error of
125 0.022 mm/s (Graziani et al., 2013, and see Table S1). The same technics can also provide an
126 almost entire removal of the ionosphere effect. An additional source of noise is due to the
127 frequency stability of the spacecraft radio-transponder. The current EnVision spacecraft design
128 foresees a stability of 0.024 mm/s (Table S1), which is about 1.7 and 4.3 times worse than the
129 Rosetta and Cassini transponder (Iess et al., 2014), respectively. However, it does not dominate
130 the Doppler noise budget even at inferior conjunction periods (Table S1). Lower-level residual
131 noise is due to the ground station Frequency and Time System (Asmar et al., 2005) and its
132 mechanical stability (Notaro et al., 2020) (Table S1). The end-to-end Doppler noise budget,
133 based on Table S1, is displayed in Figure S1 for the current design of the nominal science phase
134 of the EnVision mission starting on June 15th 2035. It shows a total floor noise of 0.043 mm/s
135 around the inferior conjunction periods and increases up to about 2.2 mm/s at the superior
136 conjunction periods (Figure S1). For comparison the X/X Doppler tracking data of Magellan had
137 an average noise around 0.1 mm/s at 10 seconds count time outside the superior conjunction
138 period (see Figure 1 in Konopliv et al., 1999).

139 3.2 The EnVision orbital motion

140 An accurate dynamical model of the spacecraft orbital motion is also important to
141 determine the gravity field of the planet (e.g. Rosenblatt et al., 2008; Marty et al., 2009;
142 Konopliv et al., 1999, 2006; Genova et al., 2016; Goossens et al., 2017). A thorough modeling of
143 all the forces driving the orbital motion of the EnVision spacecraft is taken into account. The
144 primary effect is induced by Venus' gravitational force, including the tides exerted by the Sun on
145 the planet (i.e. potential Love number k_2). The Love number k_2 has a real part and an imaginary
146 part to take into account the tidal amplitude and the effect of the tidal phase lag, respectively
147 (e.g. IERS conventions, McCarthy and Petit, 2004). The Magellan/PVO gravity solution,
148 expanded up to degree and order 180, and its associated Love number k_2 are assumed as initial
149 knowledge in our simulations. We assumed a value of 0.295 for the real part and of 0.0059 for
150 the imaginary part (i.e. tidal phase lag angle of 0.58° , corresponding to the median value of the
151 tidal dissipation factor Q values, expected from Venus interior structure models, see Figure 4 in
152 Dumoulin et al. 2017 and Table S2). The gravitational perturbations induced on the spacecraft
153 motion by the other planets of the solar system are also taken into account using a point mass
154 representation and planetary ephemerides (Folkner et al., 2013).

155 The non-gravitational forces acting on the faces of the spacecraft include the atmospheric
156 drag and the radiation pressure from the Sun and the planetary albedo and infra-red emission. A
157 single value of the albedo and of the infra-red emission are here considered. We used the VTS3
158 model (Hedin et al., 1983) for the density of the Venusian atmosphere at the altitudes of the
159 EnVision spacecraft. To compute these non-gravitational forces, we used a canon-ball shape
160 model with a surface-to-mass ratio of $0.007 \text{ m}^2/\text{kg}$, which is representative of modern spacecraft
161 design.

162 The numerical integration is performed by using these force models (hereafter *initial*
163 model) over 365 successive 4-days long data-arcs to cover the 6 Venusian days or cycles

164 duration of the EnVision mission science phase. The initial state vector at the beginning of each
165 data-arc is taken from the current design of the orbit of the EnVision spacecraft around Venus.

166 On the basis of this orbit computation, Doppler tracking data are simulated on a daily
167 basis of 3.5 hours, and the Doppler noise is modeled as a white Gaussian noise with a standard
168 deviation that accounts for the total budget and variabilities due to the SPE angle (Section 3.1).

169 3.3 Simulations of the Precise Orbit Determination process

170 A comprehensive set of numerical simulations is reported to support the science
171 investigation of the EnVision gravity experiment. The numerical simulations were carried out
172 independently with the software *Géodésie par Intégrations Numériques Simultanées* (GINS)
173 developed by the French space agency CNES (Marty et al., 2009; Rosenblatt et al., 2012) and
174 GEODYN (Pavlis et al., 2013). The simulation of the POD process consists first in building
175 Doppler measurements on the basis of the perturbation of the *initial* force model (hereafter
176 *perturbed* model) and the Doppler noise budget described in Section 3.1. The *perturbed* force
177 model takes into account as faithfully as possible the inaccuracies of the force models leading to
178 a realistic simulation of the gravity experiment.

179 The gravity field is perturbed by applying errors statistically modeled through Normal
180 distributions with a standard deviation of 1-sigma uncertainty of the Magellan/PVO gravity
181 solution (Konopliv et al., 1999) for each spherical harmonic coefficient. The real part of the Love
182 number k_2 is set to 0.1, and the imaginary part to zero. Furthermore, each non-gravitational force
183 accounts for errors by scaling randomly the *initial* model through a Normal distribution with a
184 mean value of 1 (e.g. *initial* model) and a realistic standard deviation. The radiation forces are
185 perturbed with a 0.03 standard deviation to consider possible inaccuracies in the spacecraft
186 modeling (e.g. attitude, thermo-optical coefficients of the spacecraft panels) and in the radiation
187 models. The standard deviation for the atmospheric drag is 0.3, which is representative of the
188 average fluctuations of the Venusian thermosphere density observed on the day side (~5%) and
189 night side (~50%), and is also representative of its day-to-day variability at 130-140 km (Müller-
190 Wodarg et al., 2016).

191 A further source of dynamical errors is due to Wheel-off-Loading (WoL) maneuvers
192 required to desaturate the reaction wheels used for the attitude control. These maneuvers may
193 lead to uncompensated residual velocities caused by possible thrusters' misalignment. A
194 maximum residual velocity ΔV of 1 mm/s (uniformly distributed on the along-track, cross-track
195 and radial directions) is predicted for the current EnVision spacecraft design. These effects are
196 modeled by adjusting the thrust resulting from the impulsive ΔV (Rosenblatt et al., 2004) at each
197 daily maneuver, occurring before a tracking period to enable a correct adjustment of this residual
198 ΔV effect. This scenario is in line with the requirements of the mission operations.

199 The discrepancies between the *perturbed* and *initial* (Section 3.2) model-based Doppler
200 data are then used to perform a least-squares fit of the force models by adjusting a set of
201 parameters of these models. This fit is performed on each 4-day data-arc through a weighting of
202 the Doppler data based on the assumed noise model (Section 3.1). A normal matrix is obtained
203 for each arc, which contains the partial derivatives of the Doppler measurement with respect to
204 local parameters for each arc and global parameters common to all arcs. The local parameters

205 include a scale factor for the drag force and for the radiation pressure force, the initial state
206 vector and the three components of the residual thrust generated at each WoL event. The global
207 parameters are the spherical harmonic coefficients of the gravity field to degree and order 180
208 and the Love number k_2 (real part) and its phase (imaginary part). The global solution is retrieved
209 by combining the normal matrices of all the 365 simulated 4-day-arcs, which cover 6 entire
210 Venus' cycles, to estimate both local and global parameters.

211 The drag scale factor is estimated for each arc with an average value of 1 ± 0.017 (1-
212 sigma) over the mission timespan, showing that the initial drag acceleration is precisely retrieved
213 in spite of an a priori perturbation of 30%. The average value of the estimated solar pressure
214 scale factor is 1 ± 0.019 (1-sigma). This is a small improvement with respect to the 3% a priori
215 perturbation but the adjustment of this force generally displays such a performance (e.g.
216 Rosenblatt et al., 2008; Marty et al., 2009). The estimated residual thrust at each WoL event
217 correspond to residual ΔV solutions, which have accuracies better than 20%.

218 The estimated spherical harmonic coefficients of the gravity field up to degree and order
219 180, including the Love number k_2 (real and imaginary part), and their formal uncertainties (or
220 errors) are shown in Section 4 to assess the performance of the future EnVision gravity
221 experiment.

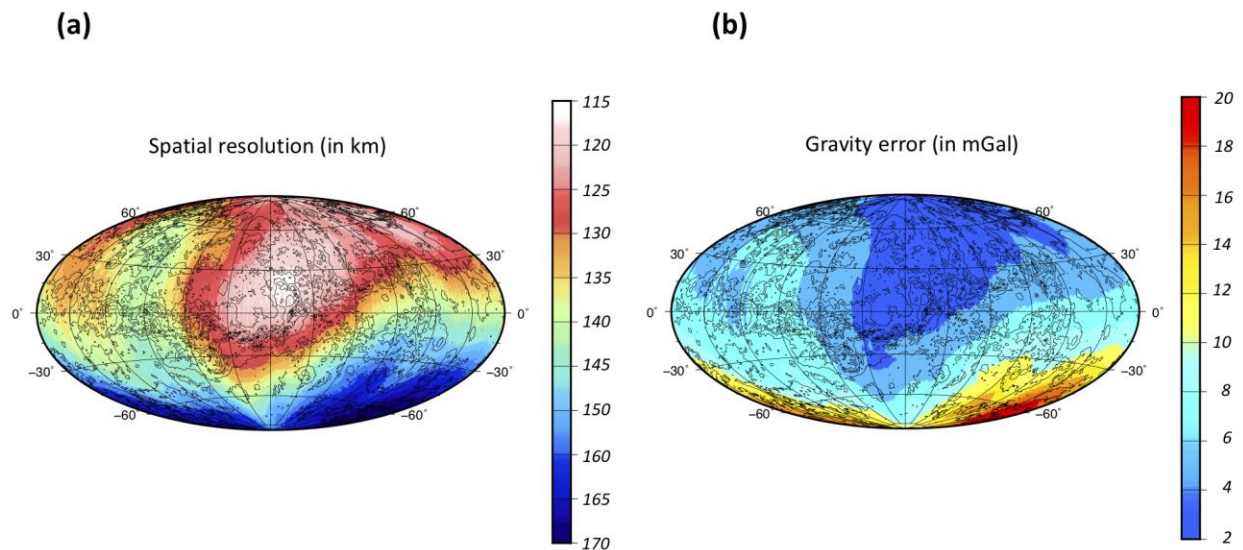
222 **4 Venus' gravity field and interior structure**

223 4.1 Static gravity and Love number k_2

224 The quality of the estimated gravity field is interpreted in terms of spatial resolution (i.e.
225 degree strength) and uncertainty. The degree strength is the harmonic degree beyond which the
226 error spectra is larger than the power spectra. Both spectra are computed with the root mean
227 square values of all the coefficients and errors at each harmonic degree (Kaula, 1966). To map
228 the spatial resolution, the local degree strength is computed from the spatially projected error of
229 the gravity solution following the method presented in Konopliv et al. (1999).

230 The minimum degree strength of the EnVision gravity solution is 110 (spatial resolution
231 of 170 km) that is obtained in the southern hemisphere (Figure 1a), and that corresponds to the
232 maximal degree obtained with the Magellan/PVO solution (in the near-equatorial areas,
233 Anderson and Smrekar, 2006). In the northern hemisphere the expected resolution of the
234 EnVision solution reaches the degree 160 that enables a spatial resolution of ~ 120 km (Figure
235 1a) over regions covered with the lowest altitude of the spacecraft orbit. The spatial resolution
236 map strongly depends, however, on the starting epoch of the science phase and on its initial
237 orbital configuration (see supporting information S1 and Figure S2)

238 To further analyze the expected accuracy of the gravity solution, Figure 1b shows the
239 gravity uncertainty map computed by considering the gravity field to degree and order 110. The
240 uncertainties are < 20 mGal everywhere and < 10 mGal for 88% of the planetary surface (Table
241 S3), respectively. This is a significant improvement over the Magellan/PVO solution, which
242 shows similar errors but at the lower degree of 70 (Konopliv and Sjogren, 1996).



243

244 **Figure 1:** Expected EnVision maps (in Hammer-Aitoff projection) of (a) the spatial resolution,
 245 and (b) the cumulated gravity error ($1-\sigma$) from the degree 2 to 110. The isocontours of the Venus
 246 topography (Rappaport et al., 1999) are shown in background.

247 The expected $1-\sigma$ error of the EnVision Love number k_2 solution is 0.001 ($\sim 0.3\%$) for the
 248 real part (Table S3), which is well within the required 3% error to improve our knowledge of the
 249 deep interior structure of the planet (Dumoulin et al., 2017). The $1-\sigma$ error of the k_2 imaginary
 250 part is 0.001, corresponding to 0.1° for the tidal phase lag error (Table S3). This error can,
 251 however, be larger because of the gravity signal due to the atmosphere (a similar issue arose in
 252 the case of Mars, Konopliv et al., 2006).

253 We also analyzed the effect of the mission duration (4 and 5 cycles or Venusian days
 254 instead of 6) on the performance of the gravity field resolution and accuracy as well as of the
 255 Love number k_2 and tidal phase lag solutions. The expected EnVision gravity solution is mainly
 256 affected if only 4 cycles of tracking data are available in the global inversion (Table S3). This
 257 degradation of the gravity field for this shorter mission duration is due to a less uniform surface
 258 coverage of the spacecraft ground tracks during tracking and an increased percentage of the
 259 noisier tracking data collected during solar conjunctions. A significant impact of the mission
 260 duration is also detected for the estimate of the Love number k_2 and tidal phase lag (Table S3).

261 4.2 Venus' interior structure

262 These significant improvements expected in the determination of Venus' gravity field
 263 will allow us to fully characterize the gravity anomalies associated with most of the geological
 264 features including large tesserae, volcanic rises and coronae. In particular, it will increase the
 265 coverage for crustal thickness estimates (Anderson and Smrekar, 2006), as well as the coverage
 266 of high-resolved gravity field above the coronae. Such a high resolution over all the entire

267 planetary surface would allow resolving gravity anomalies above more than half of the coronae.
 268 The latest gravity field solution based on the combined analysis of Magellan/POV data provides
 269 only information regarding 25% of the coronae (Hoogenboom and Houseman, 2006). This
 270 enhanced coverage of the coronae gravity signatures is required to fully understand the potential
 271 role of these structures to initiate subduction of the Venusian lithosphere (Davaille et al., 2017).

272 Moreover, a uniformly high-resolved gravity map will enable the analysis of the lateral
 273 variations of the elastic lithosphere thickness related to local heat flux variations (e.g. Smrekar,
 274 1994; Anderson and Smrekar, 2006). Was the lithosphere thinner in the past, at the time of
 275 Tesseræ formation and thicker at the time of more recent volcanic rises formation or could
 276 similar geological features form above lithosphere with various thicknesses? By addressing this
 277 outstanding question, we will be able to constrain the heat loss mechanism: episodic vs
 278 equilibrium mode or a different mode (e.g. Smrekar et al., 2018).

279 The most powerful tool to characterize the radial structure of a planet (besides
 280 seismology) is its moment of inertia, the calculation of which requires the measurement of the
 281 precession rate. The moment of inertia of Venus has been computed using estimations of the
 282 precession rate derived from Earth-based observations of radar speckles, with an uncertainty of
 283 the order of 10% (Margot, 2019). This is however not accurate enough to distinguish between
 284 the different composition models proposed in the literature for Venus that arise from different
 285 accretion scenarios (the two end-member scenarios in terms of FeO mantle content and therefore
 286 in terms of core size are the models proposed by Lewis (1972) and Ringwood (1977)). These
 287 models, combined with two different temperature profiles in the mantle (Earth-like or hotter) and
 288 assuming a core composition similar to Earth's, yield core radii from 2941 to 3425 km with
 289 corresponding moments of inertia from 0.342 to 0.327 (Dumoulin et al, 2017). In our
 290 simulations, we have introduced the estimation of the precession rate from the Envision tracking
 291 data. We found a 1- σ error of 70 arcsec.cy⁻¹, leading to a significant improvement of the error on
 292 the polar moment of inertia (1- σ =0.005, that is 1.4% of the central value of the expected range)
 293 that allows a tighter constraint on the core size.

294 As shown in Figure 2, an accuracy of less than 2% (i.e., of the order of ± 0.006) for the
 295 Love number k_2 helps to determine bounds on the core size. Assuming a fully liquid core, a
 296 small Love number k_2 (0.25-0.27) would be the signature of a core size in the lower bound
 297 (<3000 km) and of an average viscosity of the mantle larger than 10^{20} Pa s. On the contrary, a
 298 large Love number k_2 (0.33-0.35) would be the signature of a large core (>3300 km) and of a low
 299 average viscosity of the mantle (< 10^{20} Pa s). Considering a mantle composition similar to the
 300 Earth and intermediate value for mantle viscosity (10^{21} Pa s), a low value of Love number k_2
 301 (<0.27, see Dumoulin et al., 2017) would indicate that the core is entirely solid, with a viscosity
 302 in the lower bound of Earth's inner core estimates (< 10^{17} Pa s). In any case, thermal evolution
 303 modeling of mantle and core is needed in order to rule out some combinations of the state and
 304 size of the core, and of the thermal state and composition of the mantle. The determination of the
 305 tidal phase lag or Q tidal dissipation factor further constrains these parameters. The error σ_Q on
 306 Q is indeed lower than the range ΔQ for different averaged mantle viscosity values expected
 307 from Venus interior models (Table 1 and Figure S3). This expected error on Q will allow to
 308 further constrain the averaged viscosity within one order of magnitude (see figure 4 in Dumoulin
 309 et al., 2017) and along with the k_2 Love number, and the moment of inertia will allow us to place

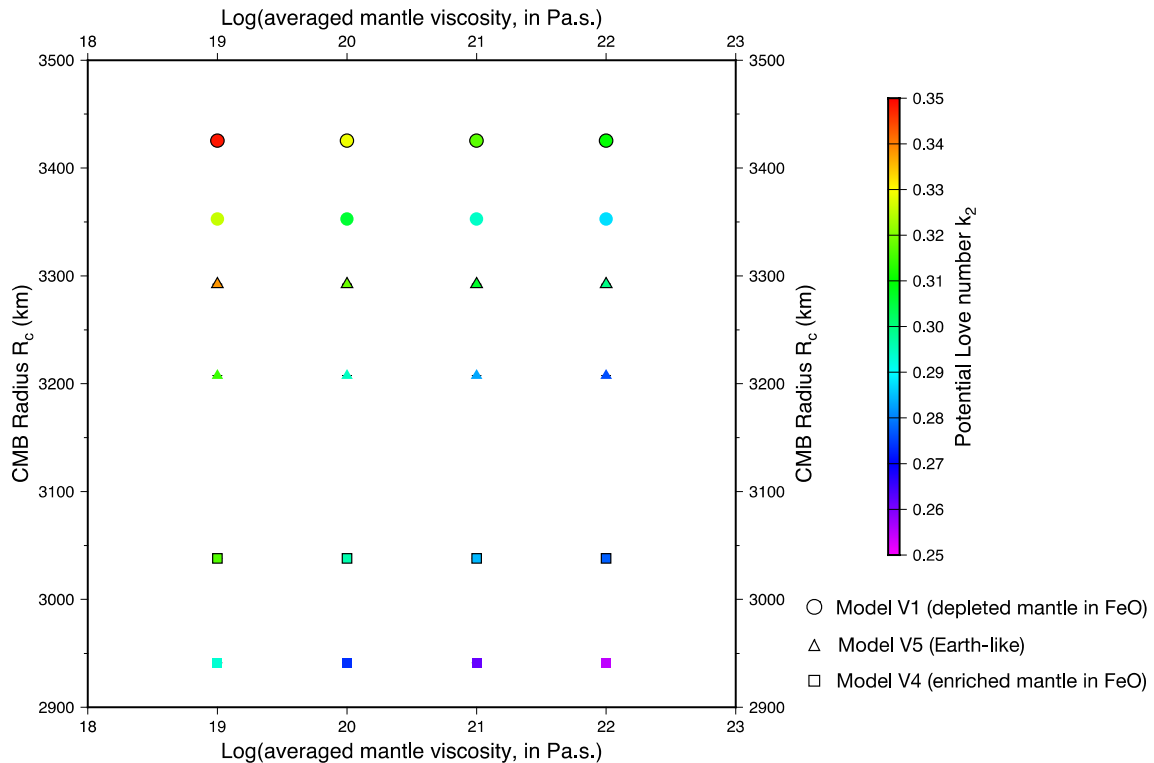
310 even more constraints on the thermal state and composition of the interior of the planet (Figure
311 2).

312 **Table 1:** Expected error (1- σ) σ_Q of the EnVision solution and theoretical range ΔQ of the
313 Venus tidal dissipation factor Q as a function of the averaged mantle viscosity (see Table S2).
314 The σ_Q error is derived from the error on the tidal phase angle $\delta\epsilon$ (0.1° or 0.0017 radian, see
315 Table S3) as follows: $\sigma_Q \approx 2Q^2\delta\epsilon$

Averaged viscosity (Pas.s)	σ_Q (<i>EnVision</i>) (1- σ)	Q +/- ΔQ (<i>Model</i>)
10^{22}	24.5	85 +/- 35
10^{21}	8.5	50 +/- 13.75
10^{20}	2.5	27.5 +/- 5
10^{19}	0.9	16.25 +/- 3.75

316

317



318

319 **Figure 2** : k_2 Love numbers computed for a viscoelastic tidal deformation of Venus as a function
 320 of the core size and the averaged mantle viscosity. Three different composition models are tested
 321 and two different temperature profiles (an Earth-like profile, symbols with contours, and one
 322 hotter, without contours). See Dumoulin et al. (2017) for a complete description of the
 323 computation method, composition models and temperature profiles.

324

325 5 Conclusion

326 The EnVision Radio-Science Experiment aims at providing a global mapping of Venus'
 327 gravity field including an accurate estimation of the gravitational tides. The experiment is based
 328 on the processing of the radio-tracking data acquired by Earth's ground stations during tracking
 329 passes dedicated to telemetry and download of the mission payload data. The numerical
 330 simulations of the EnVision mission scenario demonstrates the scientific achievements that can
 331 be accomplished by the Radio Science Experiment with the configuration under study. The
 332 resulting gravity field will provide significant accuracy and resolution refinements compared to
 333 the Magellan/PVO Venus gravity field. A better Doppler tracking noise (X/X-Ka link against
 334 X/X link on Magellan), and especially the six cycles mission duration (against the three cycles
 335 dedicated to the gravity field with Magellan) enables dramatic improvements in the knowledge
 336 of the short-wavelength gravitational anomalies. A spatial resolution of 170 km is expected
 337 globally with local resolutions of 120 km over extensive regions at mid-latitudes. This
 338 improvement will provide highly resolved gravity anomalies above most of the geological

339 features (volcanic rises, large tesserae, coronae). The improvement of the solutions of the Love
340 number k_2 (0.3% of error), of the tidal phase lag (0.1° of error) and of the moment of inertia
341 (1.4% of error) will allow us to better constrain the state and size of the core, as well as the
342 viscosity, thermal state and composition of the mantle. This improvement of the Venus interior
343 structure will then help to better constrain the thermal evolution of the planet, providing a
344 valuable contribution to the EnVision mission.

345 **Acknowledgments, Samples, and Data**

346 The Authors thank the ESA's EnVision study team for numerous and fruitful exchanges for
347 implementing the gravity experiment in the Envision mission design as well as D. Rovelli
348 (ESOC) for his valuable help to compute the Envision Doppler noise budget. This work was
349 supported by CNES during the Phase A of the EnVision mission. A.G. was financially supported
350 by the Italian Ministry of Education, University and Research (MIUR).

351 Data were not used, nor created for this research.

352

353 **References**

354 Anderson, F.S., & Smrekar, S.E. (2006). Global mapping of crustal and lithospheric thickness on
355 Venus. *Journal of Geophysical Research*, *111*(E8), 1-20. doi:10.1029/2004JE002395

356 Asmar, S.W., Amstrong, J.W., Iess, L., Tortora, P. (2005). Spacecraft Doppler tracking: Noise
357 budget and accuracy achievable in precision radio science observations. *Radio Science*,
358 *40*(RS2001), 1-9. doi:10.1029/2004RS003101.

359 Balmino, G., Moynot, B., & Vales, N. (1982). Gravity model of Mars in spherical harmonics up
360 to degree and order eighteen. *Journal of Geophysical Research*, *87*, 9735-9746.
361 doi:10.1029/JB087iB12p09735

362 Barriot, J.-P., Valès, N., Balmino, G., & Rosenblatt, P. (1998). A 180^{th} degree and order model
363 of the Venus gravity field from Magellan line of sight residual Doppler data. *Geophysical*
364 *Research Letters*, *25*(19), 3743-3746. doi:10.1029/98GL02600.

365 Davaille, A., Smrekar, S.E., Tomlinson, S. (2017). Experimental and observational evidence for
366 plume-induced subduction on Venus. *Nature Geoscience*, *10*(5), 349-355.

367 Deep Space Network note 202 (2019). Doppler tracking. *DSN 810-005, 202, Rev. C*. Pasadena,
368 CA: Jet Propulsion Laboratory.

369 Dumoulin, C., Tobie, G., Verhoeven, O., Rosenblatt, P., & Rambaux, N. (2017). Tidal
370 constraints on the interior of Venus. *Journal of Geophysical Research: Planets*, *122*(6), 1338-
371 1352. doi:10.1002/2016JE005249

372 Folkner, W.F., Boggs, D.H., & Williams, J.G. (2013). Planetary ephemeris DE430. *IOM 343-R*.
373 Pasadena, CA: Jet Propulsion Laboratory.

374 McCarthy, D.D., & Petit, G. (Eds). (2004). *IERS Conventions (2003)*, IERS Technical Note 32,
375 BKG, Frankfurt/Main.

376 Mocquet, A., Rosenblatt, P., Dehant V., & Verhoeven O. (2011), The deep interior of Venus,
377 Mars, and the Earth: A brief review and the need for planetary surface-based measurements.
378 *Planetary and Space Science*, *59*(10), 1048-1061. doi:10.1016/j.pss.2010.02.002

- 379 Genova, A., Goossens, S., Lemoine F.G., Mazarico, E., Neumann G.A., Smith, D.E., et al.
380 (2016). Seasonal and static gravity field of Mars from MGS, Mars Odyssey and MRO radio
381 science. *Icarus*, 272, 228-245. doi:10.1016/j.icarus.2016.02.050
- 382 Ghail, R., Wilson, C.F., Widemann, T., Titov, D., Bruzzone, L., Helbert, J., Vandaele, A.-C.,
383 Marcq, E., Dumoulin, C., Rosenblatt, P., and the EnVision team (2019). EnVision M5 Venus
384 orbiter proposal. *European Planetary Science Conference-Division Planetary Science joint*
385 *meeting*, Abstract#1611-2.
- 386 Goossens, S., Lemoine, F.G., Rosenblatt, P., Lebonnois, S., Mazarico, E. (2017). Analysis of
387 Magellan and Venus Express tracking data for Venus gravity field. *48th Lunar and Planetary*
388 *Science Conference*, Abstract#1984.
- 389 Graziani, A., Crewell, S., Elgered, G., Jarlemark, P., Löhnert, U., Martellucci, A., et al. (2013).
390 Media calibration system for deep space missions: Preliminary design and technical aspects. *6th*
391 *ESA International Workshop on Tracking, Telemetry and Command Systems for Space*
392 *Applications*, Darmstadt, Germany.
- 393 Ho, C.M., Morabito, D.D., & Woo, R. (2008). Solar corona effects on angle of arrival
394 fluctuations for microwave telecommunication links during superior solar conjunction. *Radio*
395 *Science*, 43(2), 1-13. doi:10.1029/2007RS003620
- 396 Holmes, D.P., Simpson, R., Tyler, G.L., Pätzold, M., Dehant, V., Rosenblatt, P., Häusler, B.,
397 Goltz, G., Kahan, D., Valencia, J., & Thompson, T. (2008). *The challenges and opportunities for*
398 *international cooperative radio science; Experience with the Mars Express and Venus Express*
399 *Missions*. Paper presented at AIAA/AAS Astrodynamics Specialist Conference 18,
400 Proceedingt#6395.
- 401 Hedin, A.E., Niemann, H.B., Kasprzak, W.T., & Seiff, A. (1983). Global empirical model of the
402 Venus thermosphere. *Journal of Geophysical Research*, 88(A1), 73-84.
403 doi:10.1029/JA088iA01p00073.
- 404 Hoogenboom, T., & Houseman, G.A. (2006). Rayleigh Taylor instability as a mechanism for
405 corona formation on Venus. *Icarus*, 180(2), 292-307. doi:10.1016/j.icarus.2005.11.001
- 406 Iess, L., Di Benedetto, M., James, N., Mercolino, M., Simone, L., & Tortora P. (2014). Astra:
407 Interdisciplinary study on enhancement of the end-to-end accuracy for spacecraft tracking
408 techniques. *Acta Astronautica*, 94, 699-707. <https://dx.doi.org/10.1016/j.actaastro.2013.06.011>
- 409 Kaula, W.M. (1966). *Theory of satellite geodesy*. Blaisdell, Waltham, M.A.
- 410 Kaula, W.M. (1996). Regional gravity fields on Venus from tracking of Magellan cycles 5 and 6.
411 *Journal of Geophysical Research*, 101(E2), 4683-4690. doi:10.1029/95JE02296.
- 412 Konopliv, A.S., & Sjogren W.L. (1996). *Venus gravity handbook. JPL publication 96-2*.
413 Pasadena, CA: Jet Propulsion Laboratory.
- 414 Konopliv, A.S., & Yoder, C.F. (1996). Venusian k_2 tidal Love number from Magellan and PVO
415 tracking data. *Geophysical Research Letters*, 23(14), 1857-1860. doi:10.1029/96GL01589
- 416 Konopliv, A.S., Banerdt, W.B., & Sjogren, W.L. (1999). Venus gravity: 180th degree and order
417 model. *Icarus*, 139(1), 3-18. doi:10.1006/icar.1999.6086

- 418 Konopliv, A.S., Yoder, C.F., Standish, E.M., Yuan, D.-N., & Sjogren, W.L. (2006). A global
419 solution for the Mars static and seasonal gravity, Mars orientation, Phobos and Deimos masses,
420 and Mars ephemeris. *Icarus*, 182(1), 23-50. doi:10.1016/j.icarus.2005.12.025
- 421 Lewis, J.S. (1972). Metal/silicate fractionation in the solar system. *Earth and Planetary Science*
422 *Letters*, 15, 286-290. doi:10.1016/0012-821X(72)90174-4.
- 423 Margot, J.-L. (2019). Earth-based radar observations of the spin axis orientation, spin precession
424 rate, and moment of inertia of Venus. *European Planetary Science Conference-DPS joint*
425 *meeting*, Abstract#412-3.
- 426 Marty, J.C., Balmino, G., Duron, J., Rosenblatt, P., Le Maistre, S., Rivoldini, A., et al. (2009).
427 Martian gravity field model and its time variations from MGS and Odyssey data. *Planetary and*
428 *Space Science*, 57(3), 350-363. doi:10.1016/j.pss.2009.01.004
- 429 Müller-Wodarg, I.C.F., Bruinsma, S., Marty, J.-C., & Hakan, S. (2016). In-situ observations of
430 waves in Venus's polar lower thermosphere with Venus Express aerobraking. *Nature Physics*,
431 12(8), 767-771. doi:10.1038/nphys3733.
- 432 Notaro, V., Iess, L., Armstrong, J.W., & Asmar, S.W. (2020). Reducing Doppler noise with
433 multi-station tracking: The Cassini test case. *Acta Astronautica*, (173), 45-52.
434 <https://doi.org/10.1016/j.actaastro.2020.04.009>
- 435 Pavlis, D. E., Wimert, J., & McCarthy, J. J. (2013). *GEODYN II System Description* (vols. 1- 5).
436 Greenbelt, MD: SGT Inc.
- 437 Rappaport, N.J., Konopliv, A.S., Kucinskis, A.B., & Ford, P.G. (1999), An improved 360 degree
438 and order model of Venus topography. *Icarus*, 139(1), 19-31. doi:10.1006/icar.1999.6081
- 439 Rosenblatt, P., Marty, J.C., Perosanz, F., Barriot, J.P., Van Hoolst, T., & Dehant, V. (2004).
440 Numerical simulations of a Mars geodesy network experiment: effect of orbiter angular
441 momentum desaturation on Mars' rotation estimation. *Planetary and Space Science*, 52(11), 965-
442 975. doi:10.1016/j.pss.2004.07.017
- 443 Rosenblatt, P., Lainey, V., Le Maistre, S., Marty, J.C., Dehant V., Pätzold, M. et al. (2008).
444 Accurate Mars Express orbits to improve the determination of the mass and ephemeris of the
445 Martian moons. *Planetary and Space Science*, 56(7), 1043-1053. doi:10.1016/j.pss.2008.02.004
- 446 Rosenblatt, P., Bruinsma, S.L., Müller-Wodarg, I.C.F., Häusler, B., Svedhem, H., & Marty, J.C.
447 (2012). First ever in situ observations of Venus' polar upper atmosphere density using the
448 tracking data of the Venus Express Atmospheric Drag Experiment (VExADE). *Icarus*, 217(2),
449 831-838. doi:10.1016/j.icarus.2011.06.019
- 450 Ringwood, A.E. (1977). *Composition and origin of the Earth*. Canberra, Research School of
451 Earth Sciences Publication No 1227, Australian National University.
- 452 Smrekar, S.E. (1994). Evidence for active hotspots on Venus from analysis of Magellan gravity
453 data. *Icarus* 112(1), 2-26. doi:10.1006/icar.1994.1166
- 454 Smrekar, S.E., Davaille, A., & Sotin C. (2018). Venus interior structure and dynamics. *Space*
455 *Science Reviews*, 214(5), 1-34. doi:10.1007/s11214-018-0518-1.

456 Zuber, M.T., Lemoine, F.G., Smith, D.E., Konopliv, A.S., Smrekar, S.E., & Asmar, S.W. (2007).
457 Mars Reconnaissance Orbiter radio science gravity investigation. *Journal of Geophysical*
458 *Research*, 112, doi:10.1029/2006JE002833.